Rheology, shrinkage, mechanical properties and microstructure of ultra-light-weight concrete with fly ash cenospheres

Zhang, Hongzhi; Ma, Wenqiang; Gao, Faliang; Ge, Zhi; Yang, Mengyu; Fang, Haibo; Šavija, Branko

DOI
10.1016/j.jobe.2024.111258

Publication date
2024

Document Version
Final published version

Published in
Journal of Building Engineering

Citation (APA)
Zhang, H., Ma, W., Gao, F., Ge, Z., Yang, M., Fang, H., & Šavija, B. (2024). Rheology, shrinkage, mechanical properties and microstructure of ultra-light-weight concrete with fly ash cenospheres. *Journal of Building Engineering*, *98*, Article 111258. https://doi.org/10.1016/j.jobe.2024.111258

Journal of Building Engineering 98 (2024) 111258

Contents lists available at ScienceDirect

Journal of Building Engineering

journal homepage: www.elsevier.com/locate/jobe

Rheology, shrinkage, mechanical properties and microstructure of ultra-light-weight concrete with fly ash cenospheres

Hongzhi Zhang [a], Wenqiang Ma [a], Faliang Gao [a], Zhi Ge [a,*], Mengyu Yang [a], Haibo Fang [b], Branko Šavija [c]

[a] School of Qilu Transportation, Shandong University, Jinan, 250002, China
[b] The Second Construction Company of China Construction Eighth Engineering Division, Jinan, 250014, China
[c] Microlab, Faculty of Civil Engineering and Geosciences, Delft University of Technology, Stevinweg 1, 2628 CN, Delft, the Netherlands

ARTICLE INFO

Keywords:
Fly ash cenospheres
Light-weight concrete
Rheology
Shrinkage
Pore structure

ABSTRACT

Cenospheres are low-density and hollow microspheres derived from coal-fired power plant fly ash waste. This study aims to prepare ultra-light-weight (<1000 kg/m^3 wet density) concrete using fly ash cenospheres (FAC). To begin with, FAC's shell thickness and the water absorption and desorption were characterized. A mixing procedure was designed to avoid the segregation between the FAC and cement slurry. FAC can affect the rheological properties of fresh mixture over time through absorption and desorption of free water. The presented ultra-light-weight concrete has several advantages compared to the ones prepared using foaming methods. First, shrinkage is significantly reduced due to FAC's internal restraint and curing effects. Secondly, it has good mechanical performance, especially in bending and is more environmentally friendly due to use of less cement. X-ray computed tomography illustrates that FAC ultra-light-weight concrete has smaller pores of more uniform size compared with those prepared using foaming methods. X-Ray diffraction, thermal gravimetry-derivative thermal gravimetry, fourier-transform infrared spectroscopy and scanning electron microscopy are employed for the hydration products and microstructure characterization. Outcomes prove that FAC can combine well with the cement matrix, and react with calcium hydroxide to produce C-A-S-H through pozzolanic reaction.

1. Introduction

Light-weight concrete is acquiring increased attention in recent construction projects (e.g., high-filled open-cut tunnel [1] and urban underground space backfilling [2]) because it has controlled density, as well as good thermal and sound insulation properties [3,4]. This material is generally composed of cementitious binder and a high degree of void space; some mixtures also contain fine aggregate [5]. In terms of binders, the most used is ordinary Poland cement (OPC). Supplementary cementitious materials (e.g., fly ash and ground blast furnace slag) are sometimes used to replace or partially replace cement [6,7].

Chemical and physical (or mechanical) methods can be used to introduce voids into the concrete matrix [5,8–10]. Chemical methods usually involve mixing H_2O_2 or aluminum powder into cement paste as gas-releasing agents. They can react to realize endogenous gas generation. These methods can reach lower density but tend to generate large voids [11]. Generally, physical methods are more commonly used in practice. The air bubbles are pre-made and mixed with matrix using a high-shear mixer [5,9]. As to the

* Corresponding author.
E-mail address: zhige@sdu.edu.cn (Z. Ge).

https://doi.org/10.1016/j.jobe.2024.111258
Received 2 August 2024; Received in revised form 22 October 2024; Accepted 5 November 2024
Available online 6 November 2024

pre-made bubbles, most are generated by a foaming agent. There are two shortcomings when using foaming agent to produce light-weight concrete. One is defoaming, the other is bubble ripening and coalescence. Both can contribute to the instability of the foam, affecting the quality of light-weight concrete. Defoaming prevents concrete from reaching to the targeted density, since less air voids are introduced. While bubble ripening and coalescence leads to large pore size occurring [12], this is harmful to mechanical performance [13]. During on-site construction, these two shortcomings may cause pore structure collapse or coalescence, leading to further problems. For example, the filling height would be reduced in backfilling construction. The phenomenon of defoaming is more pronounced in grouting construction due to the grouting pressure.

Cenospheres are produced in power plants as a byproduct of coal combustion [14]. They are spherical particles with a hollow center and belong to a kind of fly ash [15]. This property makes them popular in the field of polymers. For example, Singh et al. [16] used silver coated cenospheres along with polydopamine for thermal energy storage. Kumar et al. [17] used cenospheres to produce composite filaments with the help of 3D printed technology. The shell of cenospheres is made mainly of alumino-silicate phases, which means it has high temperature resistance. Therefore, cenospheres have been used as flame-retarding or insulation coatings [18,19]. There are also several studies of using fly ash cenospheres (FAC) in the field of construction materials. A couple of researchers used perforated or modified cenospheres as internal curing agents to improve the pore structure and improve the performance of concrete [20,21]. Baronins et al. [22] used FAC as aggregate to reduce the concrete density by 19 % (from 1790 to 1450 kg/m^3 dry density). Huang et al. [23] used FAC and fiber to make a kind of composite with the dry density of 1302 kg/m^3 and studied the behavior of fibers and cenospheres after high temperature (900 °C) treatment. Le et al. [24] used FAC to replace sand and reached a dry density of 1284 kg/m^3. These all showed the potential of using FAC to prepare ultra-light weight concrete. However, the achieved dry densities are still above 1000 kg/m^3, which is not low enough for some engineering circumstances. For example, when the light concrete serve as the backfilling material in the subgrade of highways to reduce land subsidence, the wet density should be no more than 1000 kg/m^3. What is more, limited research on the fresh properties and pore structure of the FAC ultra-light-weight concrete has been reported.

In this study, FAC was added to the cement slurry to make ultra-light-weight concrete with dry density of 626–682 kg/m^3, thereby avoiding the problems caused by foam instability. Mixtures with wet densities of 800, 900 and 1000 kg/m^3 were designed. Fresh properties, rheology, shrinkage, strength, pore structure and hydration products of the designed FAC ultra-light-weight concrete were characterized. It is believed that FAC has been successfully used to prepare light-weight concrete which can be used as a sustainable and economical solution in backfilling construction.

2. Materials and methods

2.1. Materials

Standard P·I 42.5 cement was used as binding material. Its chemical composition is listed in Table 1. Fig. 1 illustrates the particle size distribution of used cenospheres (measured by a laser particle size analyzer). Its median diameter is 729.5 μm and the specific surface area is 3.4 m^2/kg. Table 1 displays the chemical composition of cenospheres and the cement measured by X-ray fluorescence (XRF). Clearly, the cenospheres have a high silicon and aluminum content and low calcium content. Fig. 2 shows its mineral composition obtained by X-ray diffraction (XRD) analysis. The main mineral composition involves quartz and mullite. Vitreous phase is observed as well.

In addition, polycarboxylic acid superplasticizer (water reducing rate >25 %) and hydroxypropyl methylcellulose viscosity-modifying agent (VMA) were utilized to modify the flowability of fresh paste and ensure a uniform dispersion of cenospheres.

2.2. Characterization of cenospheres

2.2.1. Shell thickness measurement

In order to describe the cenospheres' shell thickness, the following operations were carried out. Initially, the cenospheres were put in a mold and impregnated using epoxy resin. Afterwards, the sample was ground by 4000 grit abrasive papers for 5 min and then polished using 3 μm and 1 μm diamond polishing pastes for 30 min, respectively. Between each grinding or polishing interval, the sample was washed in ultrasonic bath for 30 s to remove any dust from the surface [25]. Then the scanning electron microscope (SEM) was employed to obtain the backscattered electron (BSE) images (Fig. 3). Subsequently, an image processing software Image J was adopted to process the BSE images and calculate the average thickness.

2.2.2. Water absorption and desorption characteristics

A total of 50g oven-dried cenospheres was used for water absorption measurement. Cenospheres were soaked in water for 24 h. During this period, the water absorption rate of cenospheres in saturated surface dry condition was traced and water absorption curve was plotted [21,26].

Table 1
Chemical composition/%.

Component	Al_2O_3	CaO	SiO_2	SO_3	Fe_2O_3	Na_2O	K_2O	TiO_2	MnO	MgO	LOI
Cenospheres	27.42	1.90	57.51	0.19	5.59	1.53	2.93	0.96	0.07	1.46	4.41
Cement	4.43	63.10	21.31	2.30	3.61	0.17	0.77	0.27	0.05	3.29	1.48

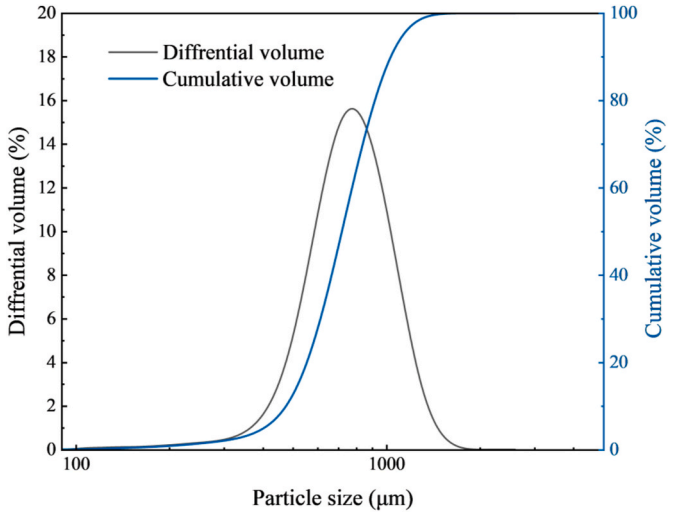

Fig. 1. Particle size distribution of cenospheres.

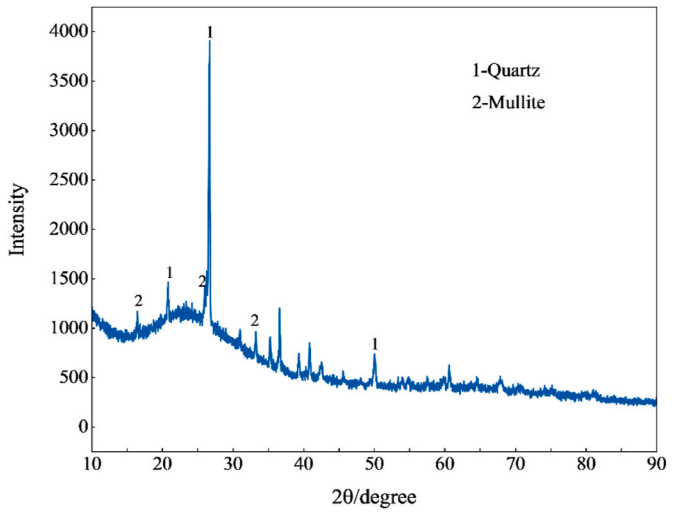

Fig. 2. XRD analysis of cenospheres.

Following ASTM E104-20 [27], saturated salt solutions were selected for the water desorption measurement, i.e., K_2SO_4 and NaBr solutions, representing the RH of 97.6 % and 59.1 %, respectively. The degressive RH can be used to simulate the decreasing moisture content occurring in the concrete matrix during hydration [20]. Both the saturated salt solution and cenospheres were placed in a sealed plastic box under a constant temperature of 20 °C to ensure a stable RH. The weight of cenospheres was measured every week until it became constant. The water desorption curve was also plotted.

2.3. Cenospheres ultra-light-weight concrete

2.3.1. Sample preparation

The water to cement ratio was 0.8 for all mixes. The wet density of cenospheres lightweight concrete was designed as 800 kg/m^3, 900 kg/m^3 and 1000 kg/m^3 by adjusting cenospheres content. Superplasticizer and viscosity-modifying agent were used to modify the flowability, and a mixing procedure [28,29] was designed, see Fig. 4.

Dry density of the specimens was measured after curing under standard conditions (RH 95 %, curing temperature 20 ± 2 °C) for 28 days. Specimen was dried in an oven at 60 °C until a constant weight. The dry density of each proportion is listed in Table 2.

2.3.2. Test methods

In the fresh state, flowability was tested using a mini slump flow measurement as follows [30]: the fresh paste was poured into a Φ80 × 80 mm open-ended cylinder, and the cylinder was then lifted vertically within 3 s. The average spread of the paste was

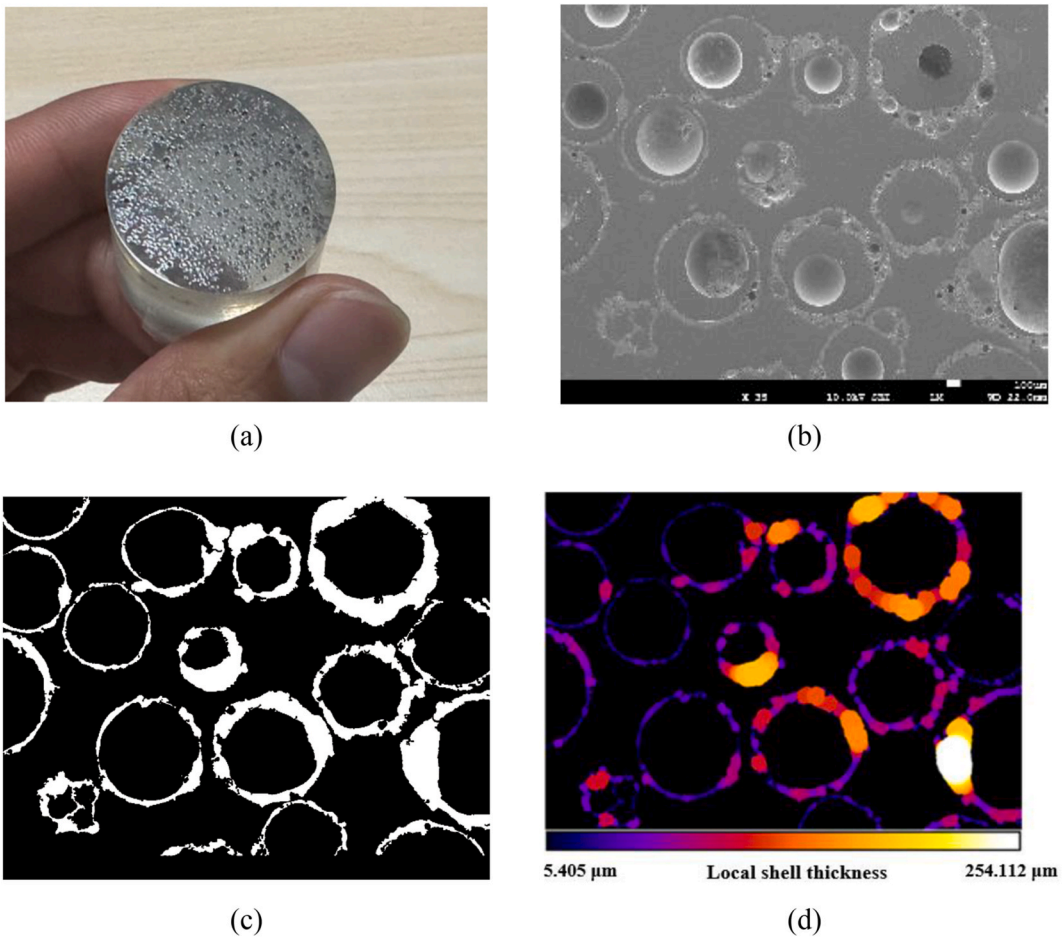

Fig. 3. The operations to get shell thickness of cenospheres: (a) cenospheres embedded in epoxy resin after polishing; (b) BSE image of the polished surface; (c) binary image (white: cenospheres shell; black: epoxy resin); (d) Spatial distribution of cenospheres thickness obtained by Image J.

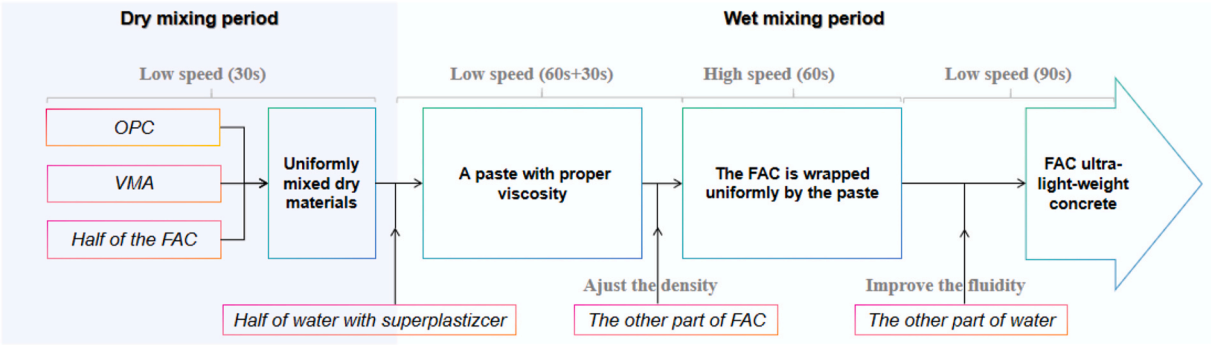

Fig. 4. The mixing procedure.

Table 2
Mix proportions of cenospheres lightweight concrete.

Wet density (kg/m³)	OPC (kg/m³)	Cenospheres (kg/m³)	Water (kg/m³)	Superplasticizer (%)	VMA (%)	Dry density (kg/m³)
1000	432	222	346	0	0.42	682
900	370	234	296	0.32	0.27	643
800	311	240	249	0.3	0.14	626

measured. Rheology test was carried out through the RSX rheometer. Fig. 5 shows the shear procedure used in the test. In the pre-shear period, the shear rate was first increased from 0 to 50 s^{-1} in 75s and then kept constant for 15s, and reduced to 0 s^{-1} in another 75s. This period is to create uniform paste conditions before the test [31]. In the data-logging shear period, the shear rate was first increased from 0 to 50 s^{-1}, and then reduced to 0 s^{-1}. The shear stress-shear rate curve obtained in the last 75s (the decreasing stage) was used for evaluating the rheological properties of the blends [32].The above shear procedure was executed at 15, 45, 75 and 105 min after the water was added to investigate the time-dependent rheological properties [32–34].

The volume stability involved autogenous deformation and drying shrinkage measurements. Autogenous deformation was measured according to ASTM C1698-2009(2014) [35]. Fresh mixtures were immediately poured into corrugated plastic tubes (420 mm in length, 29 mm outer diameter) after mixing. Three replicate specimens were tested for each wet density, and the data was collected every 15 min. Drying shrinkage was tested following the Chinese standard GB/T 11969-2020 [36]. 3 prisms with size of 40 mm × 40 mm × 160 mm were prepared for each mix. The specimens were first soaked in water (20 ± 2 °C) for 72 h. Then, the initial length and weight were recorded. The specimens were then moved to a constant temperature and humidity chamber (20 ± 2 °C, 45 ± 5%RH). The length and weight were measured every day in the first 5 days and then every 4 days. The test was terminated after the weight change was less than 0.1 %.

The compressive strength at 3, 7 and 28 days were measured following the Chinese standard JG/T 266–2011 [37]. 3 cubic specimens with size of 100 mm were loaded for each mixture using a universal loading machine at a loading rate of 2.5 kN/s 28-day flexural strength was obtained using the specimen with size of 40 × 40 × 160 mm.

The pore structures were characterized using a combination of X-ray computed tomography and image analysis technique. In this approach, a cylindrical specimen with a diameter of 50 mm and height of 150 mm was used for acquiring raw greyscale X-CT images through a high resolution micro-XCT system (ZEISS Xradia 510 Versa). The voxel size was 25 μm. A deconvolution approach was adopted to fit the greyscale value histogram by two Gaussian distributions (Fig. 6). The threshold grey value between pore and solid phases was defined as the intersection of the two Gaussian curves [38]. A comparison between a raw greyscale image and segmented binary image is given in Fig. 7.

The hydration products were analyzed using X-Ray Diffraction (XRD), Thermal gravimetry-derivative thermal gravimetry (TG-DTG) and Fourier-transform infrared (FTIR) spectroscopy. The XRD diffraction angle ranged from 5° to 90° with a step size of 0.05° at a scanning rate of 5° per minute. The TG-DTG experiments were conducted in nitrogen atmosphere and heated up from room temperature to 1000 °C using a heating rate of 10 °C min^{-1}. FTIR spectra were detected with 4 cm^{-1} resolutions, in the range of 4000∼400 cm^{-1} IR absorption band.

Scanning electron microscopy (SEM) was used to observe the morphology of hydrates and the interface between the cenospheres and hydrated cement paste. Both secondary electron (SE) and backscattered electron (BSE) modes were employed. For the BSE mode observation, the sample was impregnated and well-polished following the procedure presented in Ref. [25]. After BSE imaging, Energy Dispersive Spectrometer (EDS) mapping and line scanning were performed.

3. Results and discussion

3.1. Shell thickness

18 processed binary images including 243 cenospheres particles were used to calculate the average shell thickness using Image J.

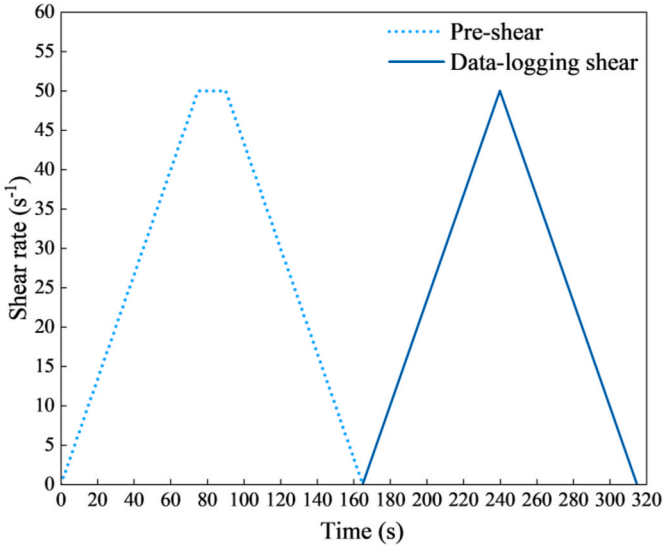

Fig. 5. The shear procedure used in the rheological property test.

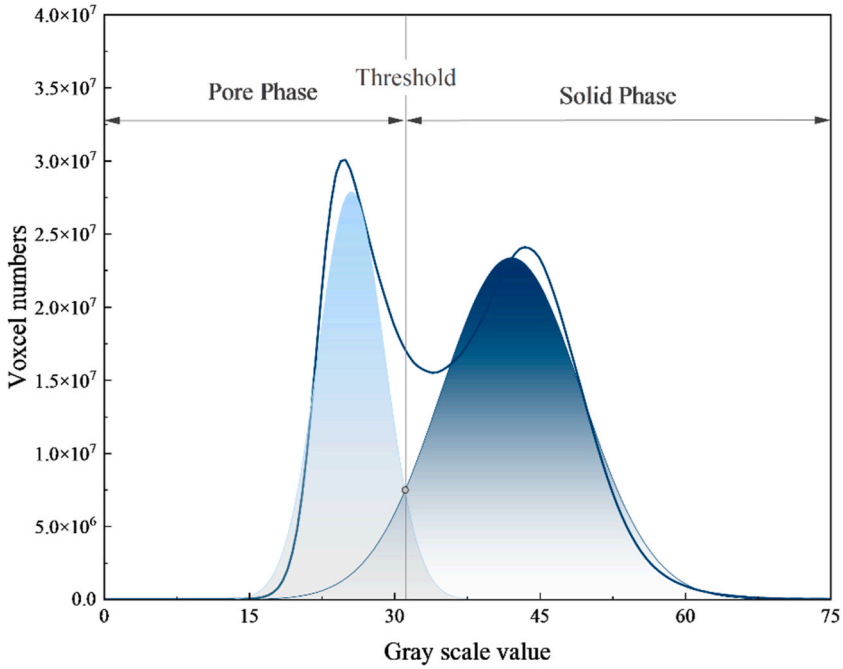

Fig. 6. Fitting the greyscale value histogram by two Gaussian distributions.

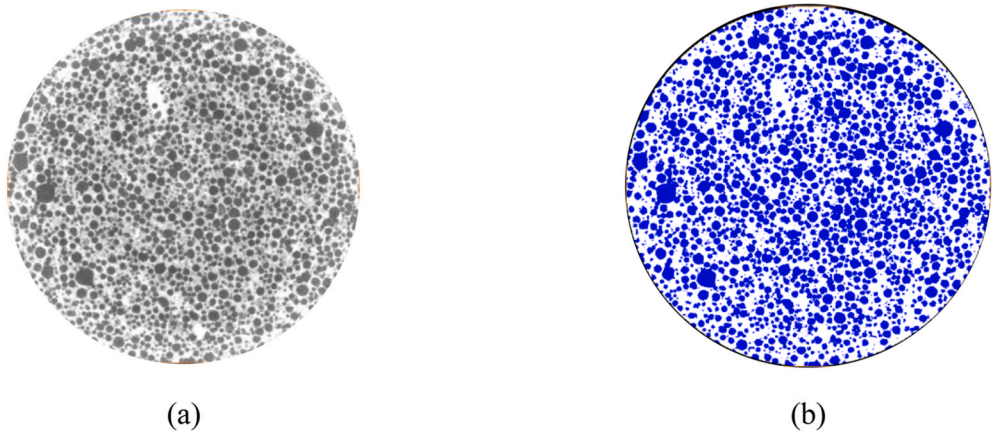

Fig. 7. The definition of the threshold grey value. (a) raw grey scale image; (b) binary image after thresholding (the blue part represents the pores). (For interpretation of the references to colour in this figure legend, the reader is referred to the Web version of this article.)

The results (Fig. 8) indicate that the shell thickness follows a Gaussian distribution and concentrates in the range of 0–150 μm. The average shell thickness is 66.4 μm. Along with the average particle size, the average internal diameter and inner volume of FAC are calculated. They are 596.7 μm and 0.11 mm^3, respectively.

3.2. Water absorption and desorption

Fig. 9 shows the water absorption and desorption curve of FAC. The water absorption of FAC increases dramatically in the first 5 h, and quickly reaches a steady level at 38 %. On the other hand, the water desorption shows a different pattern, which lasts much longer-about 80 days. FAC in low RH condition has larger water desorption. This means that the desorption period of FAC would last quite long in hydrated cement paste.

3.3. Stability of the prepared FAC ultra-light-weight concrete

Table 3 shows the measured fresh properties of FAC ultra-light-weight concrete. A density ratio is defined as the measured wet

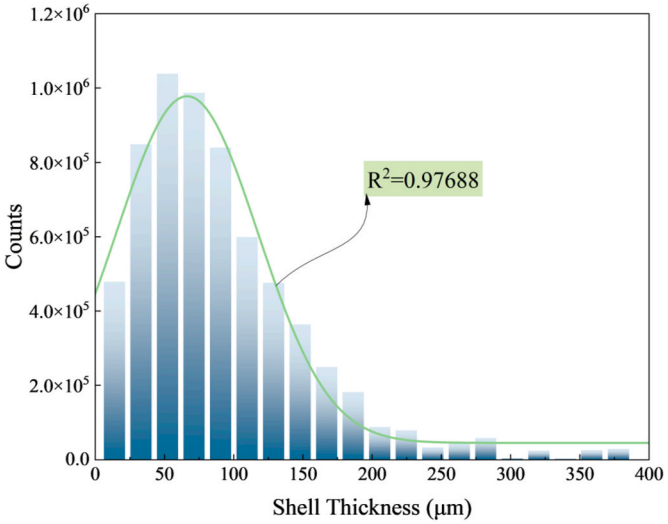

Fig. 8. Frequency of measured shell thickness.

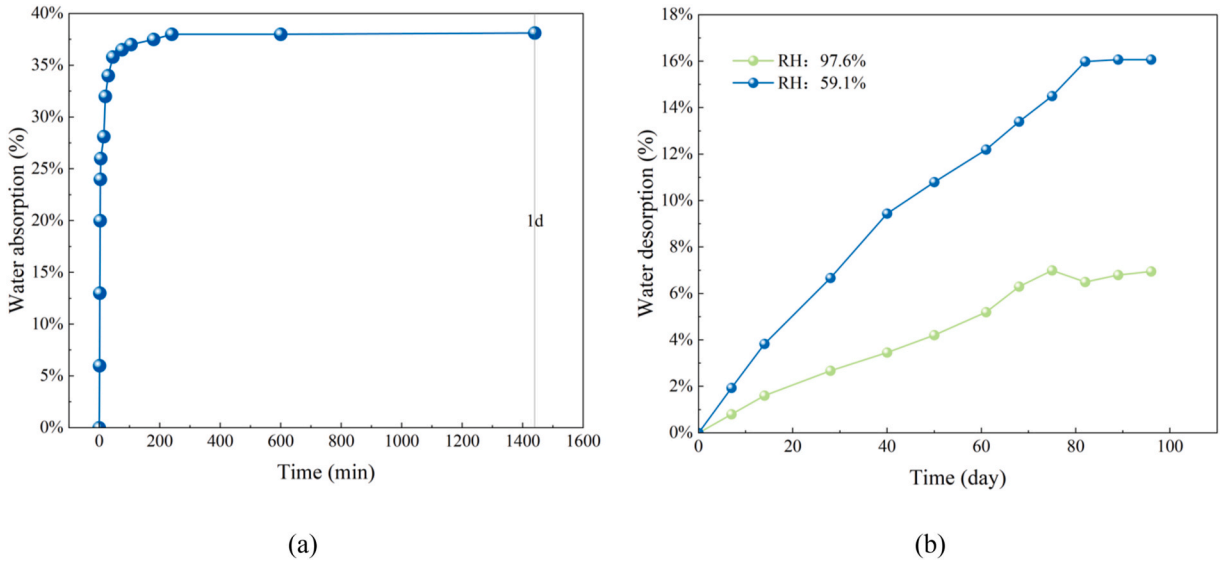

Fig. 9. Water absorption and desorption curve of FAC. (a) absorption curve; (b) desorption curve.

density/designed wet density. As listed in the table, these ratios are all nearly 1 which means that the fresh mixtures are well mixed [39–41]. Furthermore, the flowability of the mixture was controlled between 160 mm and 190 mm, in line with the requirements of in-place casting [30].

3.4. Rheology

Modified Bingham model (M − B model) was used to fit the data, and the results are shown in Figs. 10 and 11. The equation of the M − B model [42,43] is as bellow:

Table 3
Measured fresh properties of the FAC ultra-light-weight concrete.

Designed wet density (kg/m^3)	Measured wet density (kg/m^3)	Density ratio	Flow value (mm)
1000	995	0.995	171
900	920	1.022	175
800	830	1.037	164

$$\tau = \tau_0 + \eta\gamma - c\gamma^2 \quad (1)$$

where τ refers to shear stress (Pa), τ_0 refers to yield stress (Pa), η refers to plastic viscosity (Pa·s), γ refers to shear rate (S^{-1}), and c is a constant parameter.

For yield stress, from Fig. 11a, it can be found that the yield strength of 900 kg/m^3 mixture is much lower than the other two wet densities. This can be explained as follows. For one thing, more superplasticizer is added in the mixture, which can reduce the yield strength [44]. Secondly, it is very likely that the FAC dosage in 900 kg/m^3 mixture is optimum for the formation of water film. Specifically, there is not so much FAC to absorb substantial amount of water like the 800 kg/m^3 one at early stage, while can release much more water than the 1000 kg/m^3 one at later stage. That is to say the free water in the mixture can always stay at an adequate level for the water film formation. It has been reported in Ref. [31] that a thicker water film leads to a smaller yield stress.

What is more, it can be observed that the yield stress of 800 and 900 kg/m^3 first increased and then decreased slightly over time. This probably because the free water was first absorbed by the cenospheres and some of them would be released with the cement hydration going on. However, the mixture with wet density 1000 kg/m^3 does not follow the trend described above, its yield strength increases steadily with time, see Figs. 10 (c) and Fig. 11 (a). This can because, as it contains less cenospheres, the absorption and desorption have limited effects on the yield stress.

For plastic viscosity, it is the measure of the friction force in the slurry [43,45]. It increases with the increasing wet density. This is understandable because more VMA are added when the wet density increases, as shown in Table 2.

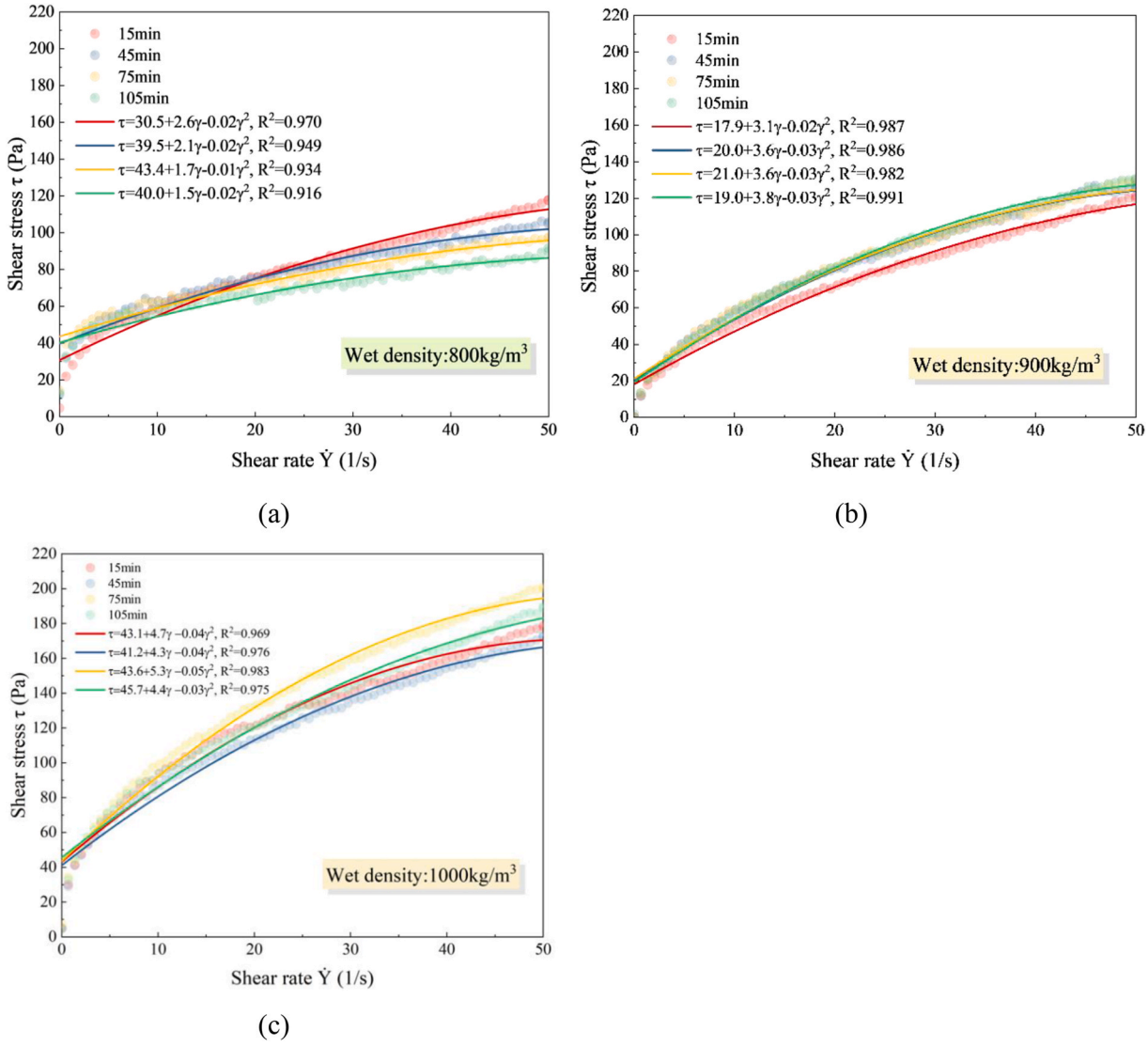

Fig. 10. Fitting of M − B model for FAC ultra-light-weight concrete: (a) 800 kg/m^3; (b) 900 kg/m^3; (c) 1000 kg/m^3.

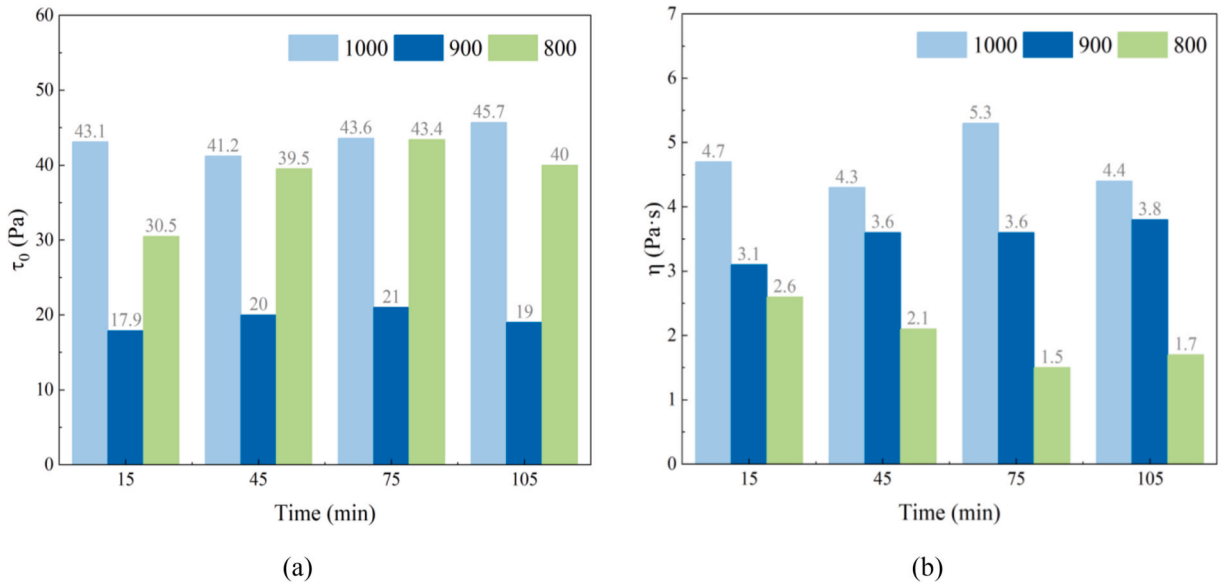

Fig. 11. The time-dependent rheological properties for FAC ultra-light-weight concrete with different wet densities: (a) yield stress τ_0; (b) plastic viscosity η.

3.5. *Volume stability*

Fig. 12 shows the autogenous deformation of FAC ultra-light-weight concrete with different wet densities. They all shrink at the first day and starts expanding afterwards. In the shrinking stage, the deformation of the 3 mixtures reaches the maximum of approximately 300 μm/m (900 kg/m^3), 400 μm/m (800 kg/m^3) and 500 μm/m (1000 kg/m^3) shrinkage strain dramatically. These values are slightly higher than the ultra-light-weight concrete in other studies [46–48] at the same age. However, the deformation is mitigated and then prominent expansion is observed after 2 days. There are two reasons for this. First, as discussed in section 3.2, the FAC can absorb water very quickly and release water slowly and steadily. When it absorbs water, the shrinkage stress caused by the capillary pores increases and shrinkage occurs; when it releases water, the matrix takes in the water and expands, as documented in Ref. [49]. Because the water desorption is a long process, the expansion also increases correspondingly. Second, the w/c ratio of this current study is 0.80, which is much higher compared with those commonly used (about 0.3–0.5). This can reduce the capillary pressure caused by the water loss [50].

Fig. 13 illustrates the drying shrinkage of the FAC ultra-light-weight concrete with different wet densities. They have a similar changing trend; the drying shrinkage first increases and then levels off at a certain value after 28 days. Drying shrinkage of FAC ultra-

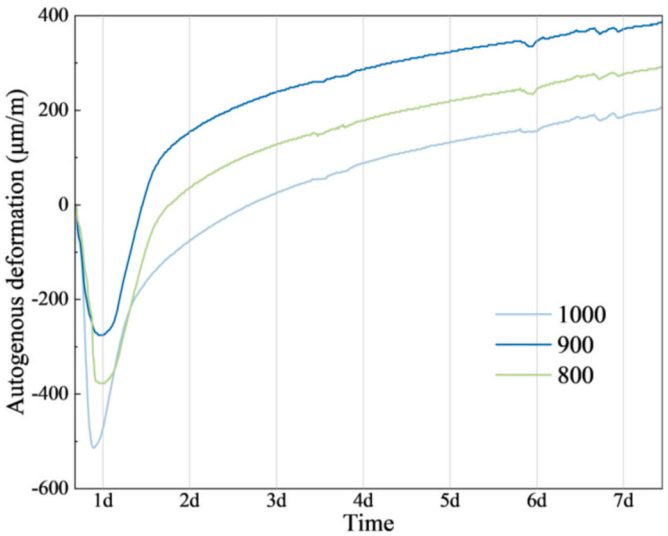

Fig. 12. Autogenous deformation of FAC ultra-light-weight concrete.

light-weight concrete is much smaller than the ones using the foaming methods [30,51,52]. For example, when the wet density is 800 kg/m^3, it is 50 % lower than the light-weight concrete in Ref. [30]. What is more, drying shrinkage decreases with the increasing FAC contents, which is consistent with the previous research [24], while the final drying shrinkage in Ref. [24] is even smaller due to the addition of shrinkage reducing mixture and PP fiber. However, there is no doubt that FAC can mitigate the drying shrinkage which can be attributed to the internal restraint [53–55] and internal curing effects [56].

3.6. Strength

As shown in Fig. 14, compressive strength increases gradually with curing age and wet density, as expected. Table 4 compares the FAC ultra-light-weight concrete in this study and the ones formed by other methods [38,57–59]. Overall, the 28-day compressive strength of FAC ultra-light-weight concrete is slightly lower (about 10%–20 %) than the others reported in the literature [38,57–59]. However, in terms of the flexural strength, it can exceed that of the light-weight concrete foamed by protein-based anionic foaming agent. This can be explained as follows. Firstly, cenospheres has coarse surface which is beneficial to the tight bond between cement matrix and cenospheres. Second, as shown in Fig. 15, the FAC can disturb the propagation of cracks leading to a more tortuous crack pattern, increasing the size of fracture process zone, thus resulting in a higher flexural strength [60].

Furthermore, the FAC ultra-light-weight concrete consumes much less cement when the targeted wet density is the same compared to (traditional) foam concrete. It has the highest strength-to-cement content ratio among them (see Table 4). This value can be used to evaluate the environmentally friendly performance of the light-weight concrete because when the required strength is fixed, less cement consumption leads to lower embodied energy and CO_2 emissions [61,62]. In other words, FAC ultra-light-weight concrete is a more environmental-friendly porous material.

3.7. Pore structure

Fig. 16 shows the pores spatial distribution of the prepared ultra-light-weight concrete segmented from the X-CT images. Note that the FAC shell cannot be identified as it has similar density as the hydrated cement paste. The pore phase mainly represents the inner volume of FAC and air voids involved during mixing.

The average porosity along the height (Z-direction) of each mix is present in Fig. 17a. The slice porosity fluctuated around the average porosity, which reflected that the cenospheres are well-distributed in the cement matrix. The average porosity decreases when wet density increasing. It is 51 %, 39 % and 25 % for specimen with density of 800 kg/m^3, 900 kg/m^3,1000 kg/m^3, respectively. Fig. 17b shows that the equivalent pore diameters. They are all smaller than the calculated FAC internal diameter in section 3.1. High-density FAC concrete has smaller pore size and narrower pore size distribution. These could be explained by the fact that high-density FAC concrete contains more hydrated cement paste, and most pores existing in cement are smaller than that of FAC. Compared with the ultra-light-weight concrete (protein-based anionic foamed) in Ref. [38], FAC ultra-light-weight concrete has much larger porosity but smaller equivalent pore size. This means FAC ultra-light-weight concrete has a more stable structure.

3.8. Hydration products

XRD patterns of the hardened FAC ultra-light-weight concrete is shown in Fig. 18. Hydrates of ettringite, Ca $(OH)_2$ and calcium

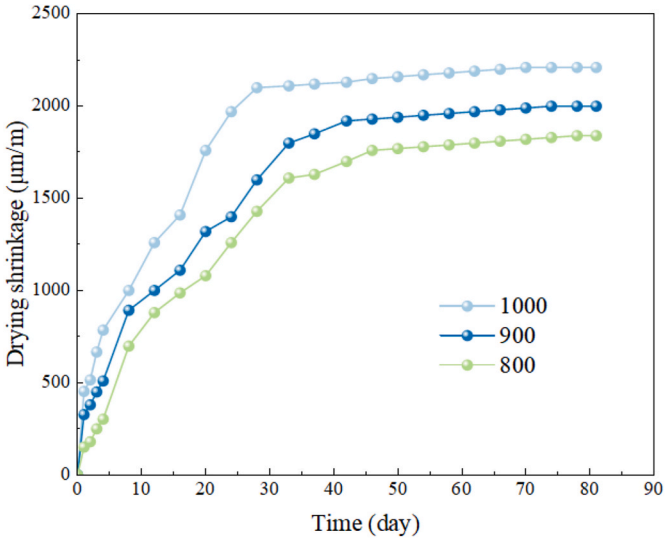

Fig. 13. Drying shrinkage of FAC ultra-light-weight concrete.

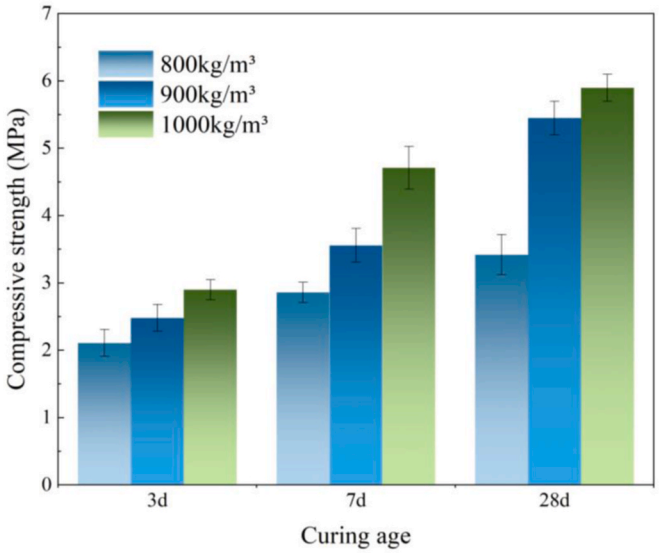

Fig. 14. Compressive strength of FAC ultra-light-weight concrete.

Table 4
The comparation between FAC ultra-light-weight concrete and other kind of light-weight concrete.

Relevant works	w/c ratio	Target wet density (kg/m^3)	28-d compressive strength (MPa)	28-day flexural strength (MPa)	cement content (kg/m^3)	foaming method	strength-to-cement content ratio (MPa·kg^{-1}·m^{-3})
Jiang et al. [38]	0.50	800	3.74	1.26	521	physical (protein-based anionic foaming agent)	0.007
Li et al. [57]	0.40	800	4.35	/	593	physical (SDS anionic surfactant foaming agent)	0.007
Wu et al. [58]	0.93	/	3.62	/	425	chemical (alumina power)	0.008
Huang et al. [59]	0.78	250	0.68	/	91	chemical (H_2O_2)	0.007
Current study	0.80	800	3.42	1.64	311	physical (cenospheres)	0.011

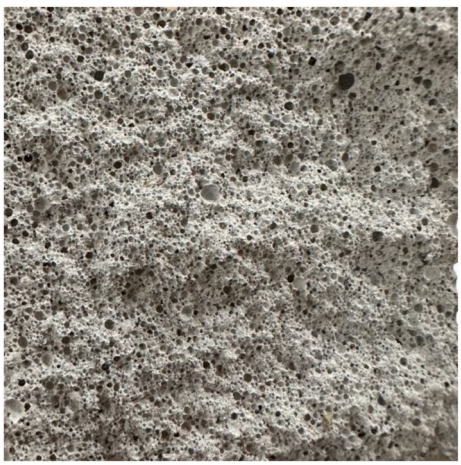

Fig. 15. The fracture surface of FAC ultra-light-weight concrete.

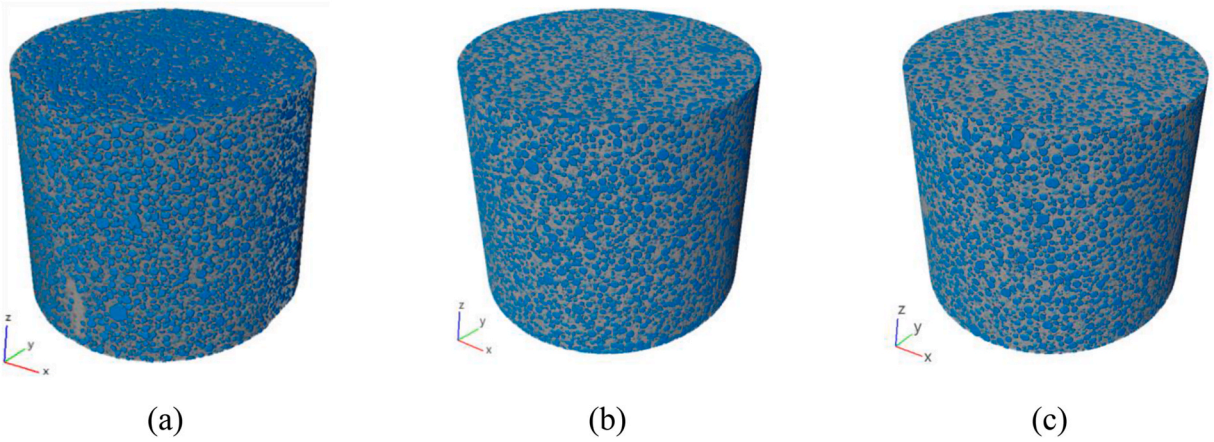

Fig. 16. Spatial distribution of pore phase in the region of interest (Φ25*20 mm) of scanned FAC ultra-light-weight concrete. (a) 800 kg/m^3; (b) 900 kg/m^3; (c)1000 kg/m^3.

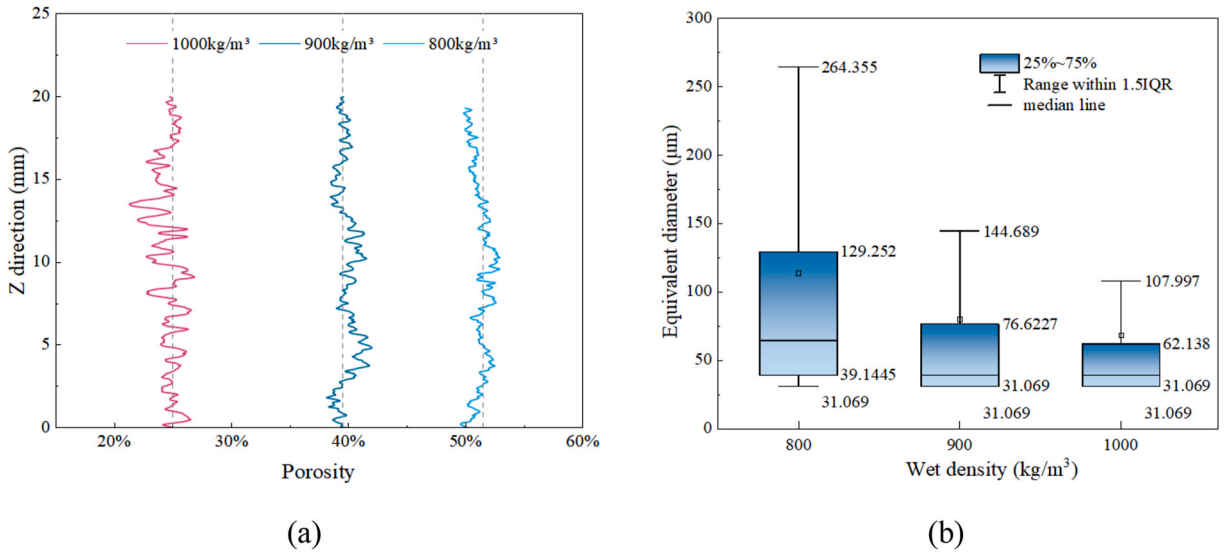

Fig. 17. X-CT analysis outcomes. (a) The average porosity of the scanned slices of X-CT image along Z direction; (b) the equivalent diameter of different wet densities.

silicate are detected. The peak intensity of hydrates increases with the wet density and curing age. C-A-S-H is detected as well, which reveals that the aluminum phase of FAC can participate in the hydration process.

Fig. 19 shows the results of the FTIR. The hydration products of different wet density are the same. The wavenumbers, 970 cm^{-1} and 455 cm^{-1} represent the Si-O stretching in Q2 site and Si-O bending, respectively; 660 cm^{-1} represents Si-O-Si bending. These 3 bands indicate that C-S-H is included in the hydration products [63–65]. The peak at 455 band become more remarkable with curing age growing, this is consistent with the results of XRD analysis. Besides, it has been reported that the characteristic peaks of gel phases are similar and can overlap with each other [64,65]. Hence, other gels like C-A-S-H cannot be distinguished from the measurement.

The outcomes of TG-DTG are shown in Fig. 20. The decomposition peak of C-S-H, ettringite and CH are about 100 °C, 100 °C–150 °C and 380 °C–500 °C, respectively [66,67].

$$\text{CH}-\text{to}-\text{Cement ratio} = \frac{\text{CH content}}{\text{Cement content}} \tag{2}$$

The calcium hydroxide (CH) content (%) in hardened FAC ultra-light-weight concrete is calculated based on the method proposed in Refs. [66,67]. Cement content (%) is the proportion of cement to raw materials listed in Table 2.

CH content and CH-to-Cement ratio are all listed in Table 5. It illustrates that the higher wet density corresponds to the more CH production as it has more cement involved in the hydration. Additional, the w/c ratio of these 3 mixtures is the same, while the CH-to-cement ratio decreases with the FAC content increasing, this means FAC can consume CH through pozzolanic reaction as reported in

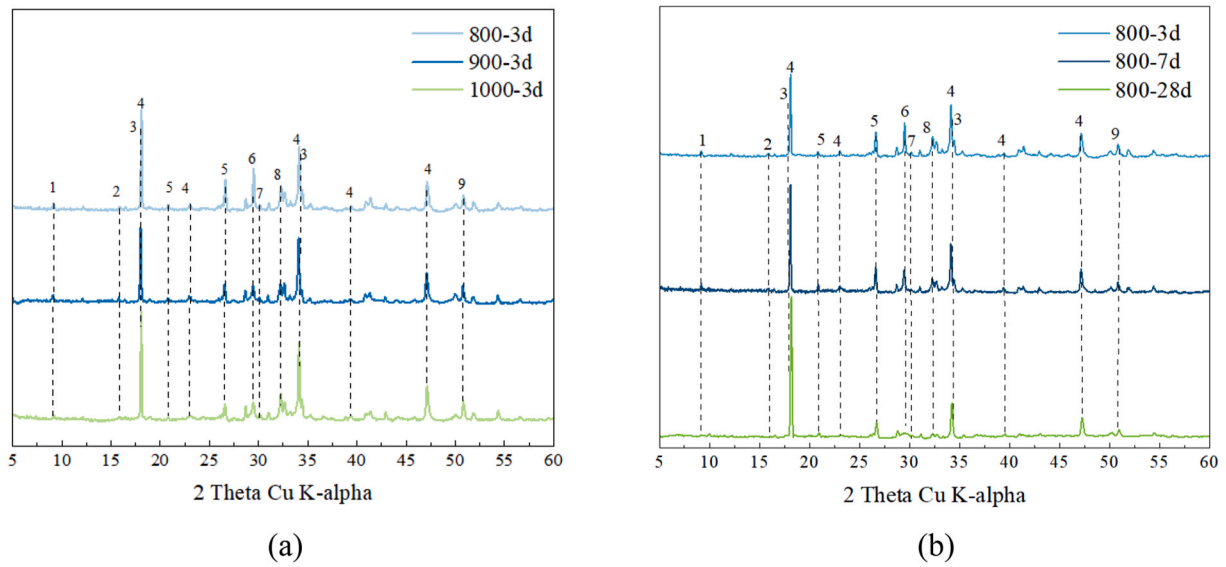

Fig. 18. XRD analysis of the hardened FAC ultra-light-weight concrete (1-ettringite 2-Mullite 3- Calcite 4- Ca $(OH)_2$ 5-Quartz 6-C_2S 7-C_3S 8-C-A-S-H 9-Calcium silicate). (a) same curing age, different wet density; (b) same wet density, different curing age.

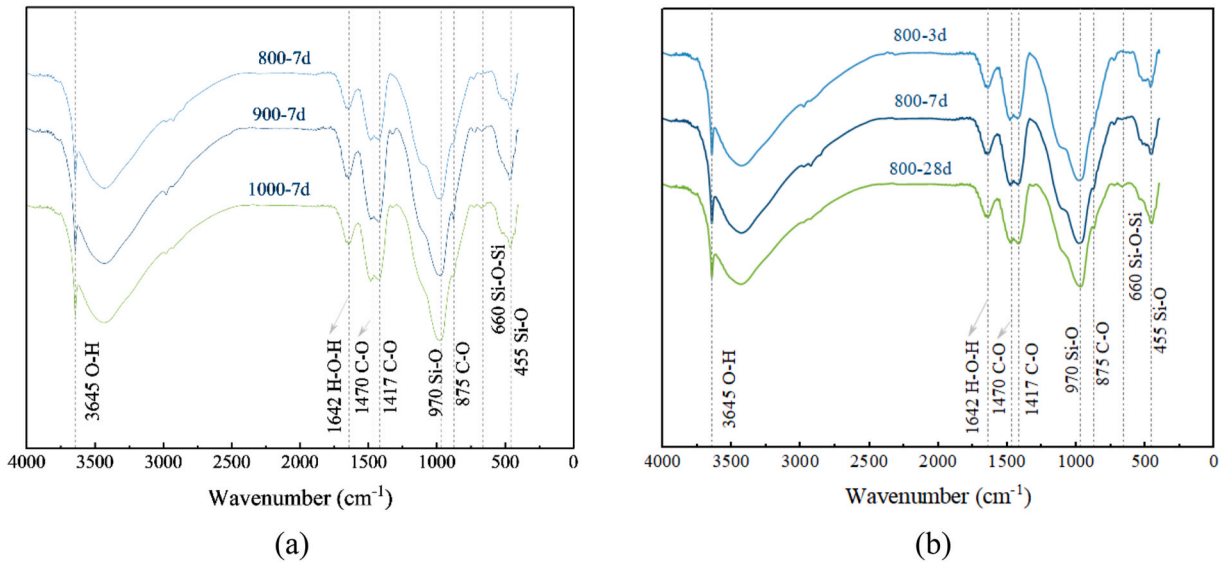

Fig. 19. FTIR analysis of the hardened FAC ultra-light-weight concrete (a) with different densities cured for 7days; (b) with density of 800 cured for 3, 7 and 28 days.

Ref. [68].

Fig. 21 is the SE image of the hardened FAC ultra-light-weight concrete. Hydrates of CH, C-S-H and ettringite can be observed. Fig. 21e illustrates that cement matrix combines well with the FAC, which is beneficial for mechanical performance.

The elemental mapping of the FAC ultra-light-weight concrete with 200 × magnification is presented in Fig. 22. In the FAC shell, Si and Al elements are high while Ca element is low, which is consistent with the test results of XRF.

In addition, in order to find out the element distribution in the interface between FAC and cement matrix, EDS line scanning was operated as shown in Fig. 23a. Fig. 23b shows the element content along the line. The ultra-light grey part represented the elements in the FAC, and the white part, the cement matrix. It can be observed that the 0-point lies in a "elements changing region", indicating that Si and Al might seep out from the shell, and Ca might migrate towards the shell. This element migrations mean the FAC is reactive and C-A-S-H gel can be possible formed.

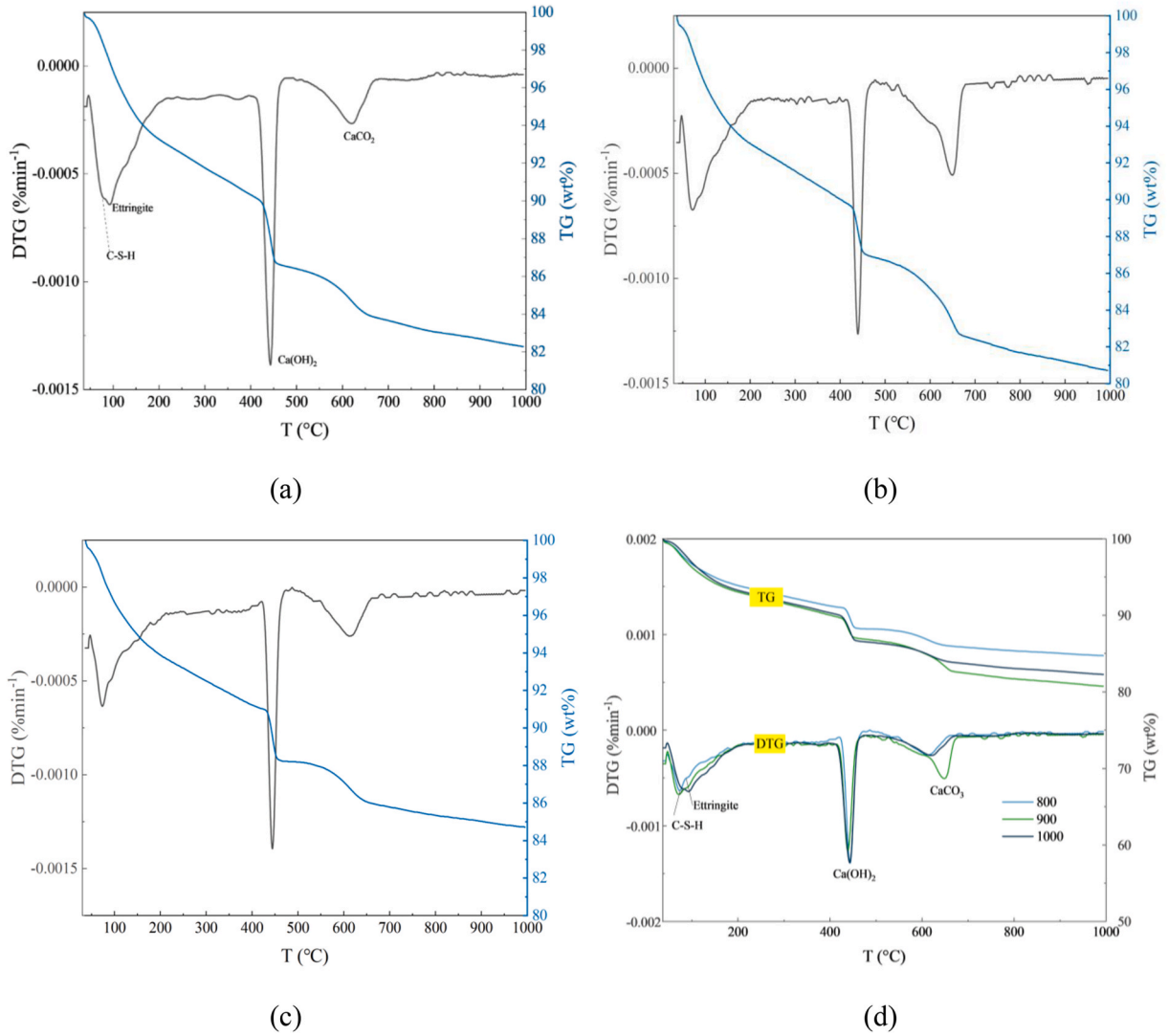

Fig. 20. TG-DTG results of the hardened FAC ultra-light-weight concrete. (a) 1000 kg/m^3; (b) 900 kg/m^3; (c) 800 kg/m^3; (d) comparison of all wet densities.

Table 5
CH content of FAC ultra-light-weight concrete of different wet densities.

Wet density (kg/m^3)	W/C	CH content (%)	CH-to-Cement ratio
1000	0.8	18.0	0.42
900	0.8	15.7	0.38
800	0.8	13.3	0.34

4. Conclusions

In this paper, FAC was mixed with cement to prepare ultra-light-weight concrete. Both the characteristics of FAC and the performance of FAC ultra-light-weight concrete were investigated. Based on the presented results, the following conclusions can be drawn.

- The FAC can absorb water quickly in the first 5 h to reach 38 % moisture content while it can release water steadily up to 16 % at an RH = 59.1 % during a quite long period (about 80 days).
- The dosage of cenospheres can have effect on the time-dependent rheological properties of the fresh mixture but only above a certain amount.

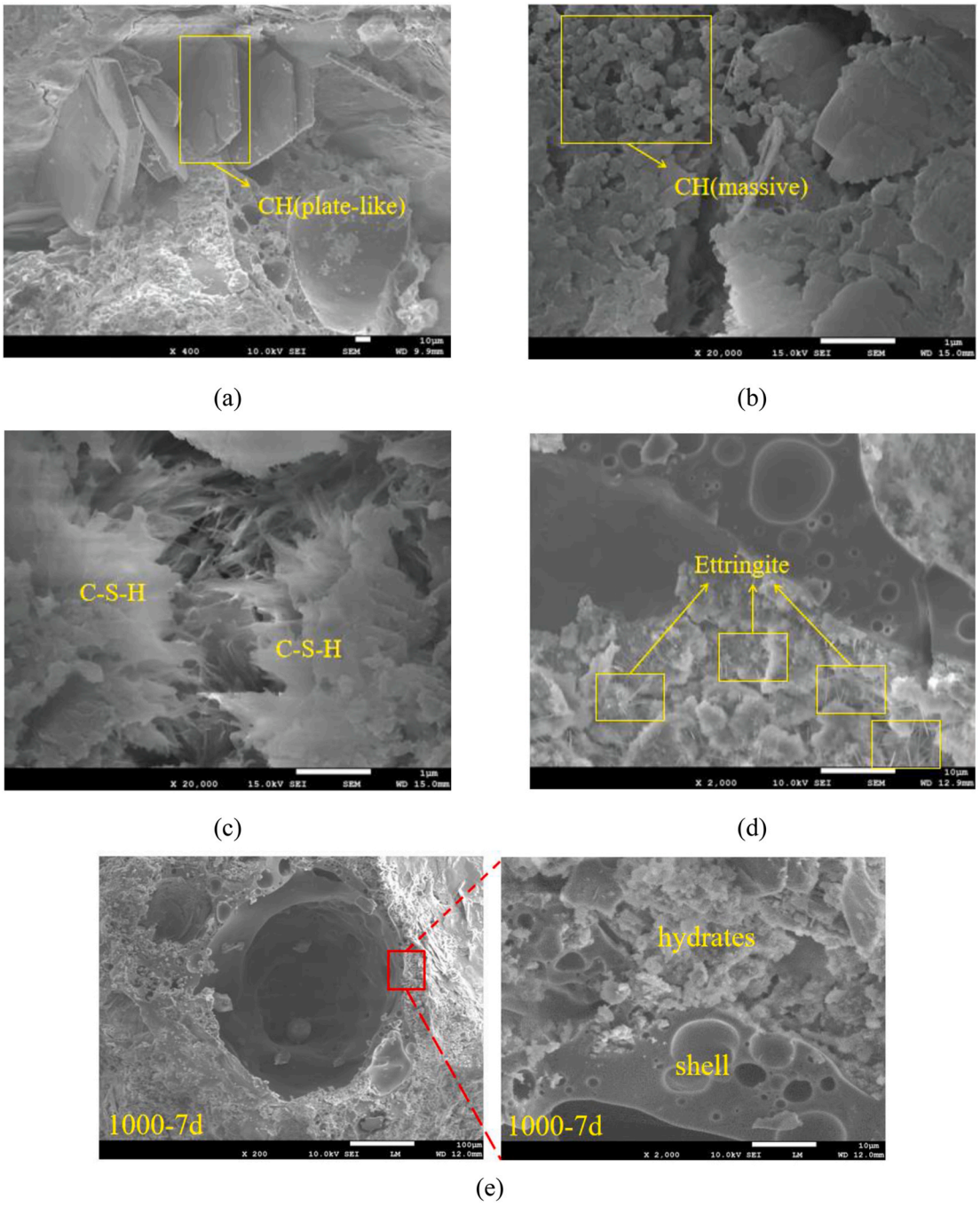

Fig. 21. SEM images of the hardened FAC ultra-light-weight concrete. (a) plate-like CH in samples of 900 kg/m^3 at 28 days; (b) massive CH in samples of 900 kg/m^3 at 28 days; (c) C-S-H gel in samples of 900 kg/m^3 at 28 days; (d) ettringite in samples of 900 kg/m^3 at 28 days; (e) the combination between FAC and hydrates.

- The FAC ultra-light-weight concrete shows good volume stability: its autogenous deformation and drying shrinkage can be mitigated due to the aggregate restriction and internal curing effects.
- FAC ultra-light-weight concrete has good mechanical properties: its 28-day compressive strength can reach 5.9 MPa. The flexural strength of 800 kg/m^3 wet density can reach 1.64 MPa. Compared with light-weight concretes created by other foaming methods of similar strength, it consumes less cement, and is thus more environmentally friendly.

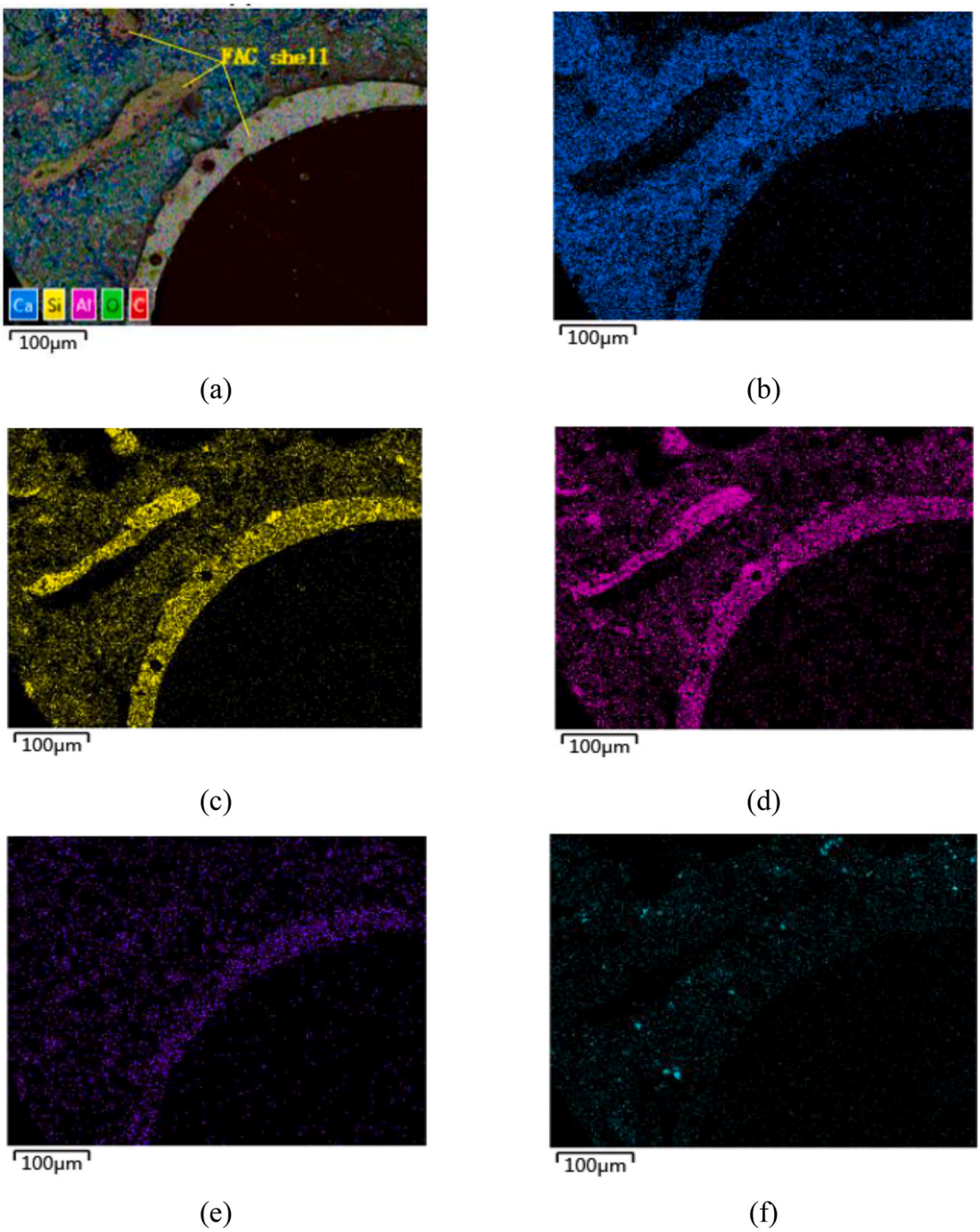

Fig. 22. EDS mappings of FAC ultra-light-weight concrete of 900 kg/m^3 at 28 days: (a) EDS image composed by different element mappings, (b) Ca mapping, (c) Si mapping, (d) Al mapping, (e) Fe mapping, (f) Mg mapping.

- Pore structure analysis indicates that cenospheres can be well distributed in the FAC ultra-light-weight concrete. The distribution of equivalent diameter is uniform. FAC ultra-light-weight concrete has larger porosity but smaller equivalent pore diameter than the protein-based anionic foamed ones.
- XRD, FTIR, TG-DTG and SEM were employed to characterize the hydration products. Ettringite and CH can be observed clearly, and the bond between cenospheres and cement matrix is strong. Furthermore, XRD and FTIR measurements illustrate that CASH gel can form, and EDS line scanning indicates that Al and Si element might seep out from the shell, while Ca element might migrate towards the shell. All these measurements prove that FAC can react with CH to produce C-A-S-H through pozzolanic reaction.

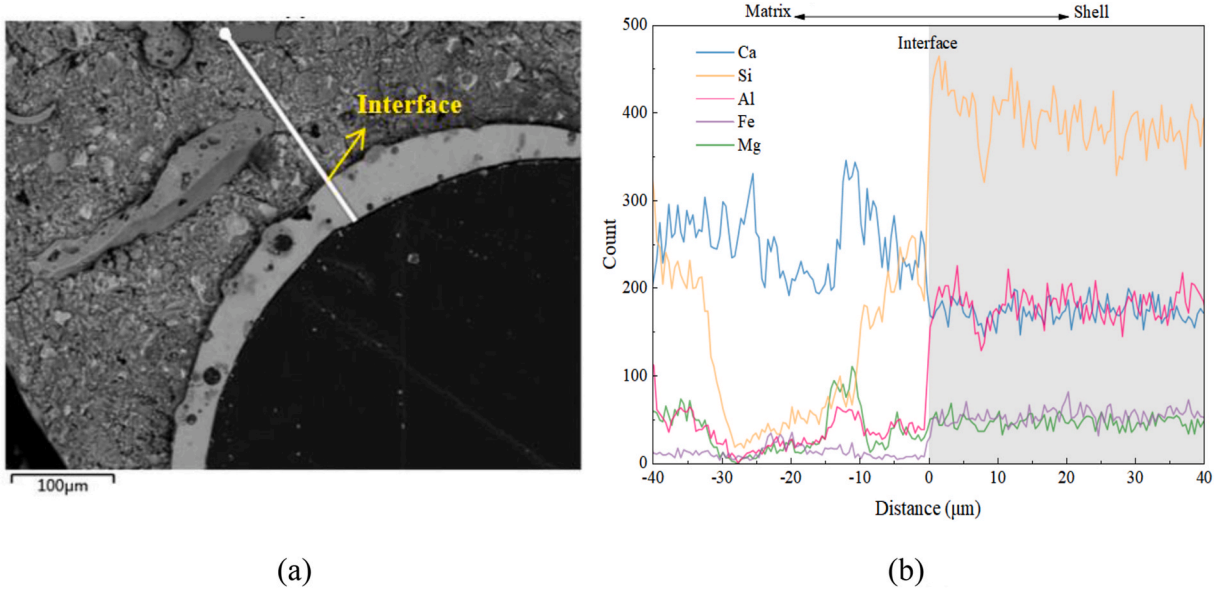

Fig. 23. EDS line scanning of FAC ultra-light-weight concrete of 1000 kg/m^3 at 28 days. (a) schematic view of the EDS line scanning; (b) element content along the scanned line.

CRediT authorship contribution statement

Hongzhi Zhang: Writing – review & editing, Supervision, Funding acquisition. **Wenqiang Ma:** Writing – original draft. **Faliang Gao:** Resources. **Zhi Ge:** Writing – review & editing. **Mengyu Yang:** Visualization. **Haibo Fang:** Resources. **Branko Šavija:** Writing – review & editing.

Declaration of competing interest

The authors declare no conflict of interest.

Acknowledgement

This work was supported by Key Basic Research Project of China (No. 2022YFC3005604), National Natural Science Foundation of China (52378250), 111 Project (No. B21012), Taishan Scholar Foundation of Shandong Province (No. tsqn201909032) and "Unveiling and Commanding" Project of Jinan Municipal Bureau of Science and Technology (202323007).

Data availability

Data will be made available on request.

References

[1] M. Li, S. Yan, S. Li, Y. Ma, L. Zhao, Z. Zhang, Study on structural mechanical behavior of secondary backfill of high filled open cut tunnelwith foamed lightweight soil, J. China Railw. Soc. 44 (2) (2022) 135–142.
[2] L.-l. Guan, Y.-g. Chen, W.-m. Ye, D.-b. Wu, Y.-f. Deng, Foamed concrete utilizing excavated soil and fly ash for urban underground space backfilling: physical properties, mechanical properties, and microstructure, Tunn. Undergr. Space Technol. 134 (2023) 104995.
[3] M.R. Ahmad, B. Chen, M.A. Haque, S.F.A. Shah, Utilization of industrial and hazardous waste materials to formulate energy-efficient hygrothermal bio-composites, J. Clean. Prod. 250 (2020) 119469.
[4] J. Shi, B. Liu, Z. He, Y. Liu, J. Jiang, T. Xiong, J. Shi, A green ultra-lightweight chemically foamed concrete for building exterior: a feasibility study, J. Clean. Prod. 288 (2021) 125085.
[5] N.B. Singh, Foamed geopolymer concrete, Mater. Today: Proc. 5 (7, Part 2) (2018) 15243–15252.
[6] X. Zhang, X. Zhang, X. Li, D. Tian, M. Ma, T. Wang, Optimized pore structure and high permeability of metakaolin/fly-ash-based geopolymer foams from Al– and H2O2–sodium oleate foaming systems, Ceram. Int. 48 (13) (2022) 18348–18360.
[7] M.R. Jones, A. McCarthy, Utilising unprocessed low-lime coal fly ash in foamed concrete, Fuel 84 (11) (2005) 1398–1409.
[8] Z. Zhang, J.L. Provis, A. Reid, H. Wang, Geopolymer foam concrete: an emerging material for sustainable construction, Construct. Build. Mater. 56 (2014) 113–127.
[9] Y. Xu, Study on the Adaptability of ChemicalFoaming Agent in Alkali Slag Cementitious Material System, Chongqing University, 2022.
[10] X. Liu, Preparation of Concrete Foam Agent Andstudy on Performance of Foamed Concrete, Chongqing Jiaotong University, 2023.
[11] A. Hajimohammadi, T. Ngo, P. Mendis, J. Sanjayan, Regulating the chemical foaming reaction to control the porosity of geopolymer foams, Mater. Des. 120 (2017) 255–265.

[12] Y. Xiong, B. Pang, Z. Liu, C. Liu, Z. Hu, L. Ma, Effect of foam temperature on foam stability of foamed concrete and stabilization mechanisms, J. Build. Eng. 77 (2023) 107492.
[13] P. Sriram Karthick Raja, T. Thyagaraj, Significance of compaction time delay on compaction and strength characteristics of sulfate resistant cement-treated expansive soil, J. Rock Mech. Geotech. Eng. 13 (5) (2021) 1193–1202.
[14] H. Li, D. Xu, S. Feng, B. Shang, Microstructure and performance of fly ash micro-beads in cementitious material system, Construct. Build. Mater. 52 (2014) 422–427.
[15] N. Ranjbar, C. Kuenzel, Cenospheres: a review, Fuel 207 (2017) 1–12.
[16] K.G.K. Singh, S. Halder, Polydopamine based silver coated cenosphere microcapsule for thermal energy storage, Mater. Today Commun. 38 (2024) 107815.
[17] J. Kumar, S. Negi, V. Mishra, 3D printed PETG/cenosphere syntactic foam composites for lightweight structural applications, Mater. Lett. 355 (2024) 135493.
[18] F. Li, Y. Wang, M. Lai, J. Zhao, Sodium lignosulfonate improves the compatibility of melamine polyphosphate with graphite-containing alkali-activated cenospheres-based coating for flame-retarding plywood, Mater. Today Commun. 36 (2023) 106450.
[19] A. Chávez-Valdez, A. Arizmendi-Morquecho, G. Vargas, J.M. Almanza, J. Alvarez-Quintana, Ultra-low thermal conductivity thermal barrier coatings from recycled fly-ash cenospheres, Acta Mater. 59 (6) (2011) 2556–2562.
[20] P. Chen, W. Tan, X. Qian, F. Yang, Y. Fang, J. Wang, M. Li, Improving the pore structure of perforated cenospheres for better internal curing performance, Mater. Des. 222 (2022) 111047.
[21] Y. Zhang, Z. Fan, X. Sun, X. Zhu, Utilization of surface-modified fly ash cenosphere waste as an internal curing material to intensify concrete performance, J. Clean. Prod. 358 (2022) 132042.
[22] J. Baronins, J. Setina, G. Sahmenko, S. Lagzdina, A. Shishkin, Pore distribution and water uptake in a cenosphere-cement paste composite material, IOP Conf. Ser. Mater. Sci. Eng. 96 (1) (2015) 012011.
[23] Z. Huang, K. Padmaja, S. Li, J.Y.R. Liew, Mechanical properties and microstructure of ultra-lightweight cement composites with fly ash cenospheres after exposure to high temperatures, Construct. Build. Mater. 164 (2018) 760–774.
[24] H. Le Viet, T. Le Trung, T. Nguyen Van, Experimental study on drying shrinkage of structural lightweight concrete using fly ash cenospheres, GEOMATE Journal 21 (87) (2021) 95–101.
[25] M. Liang, S. He, Y. Gan, H. Zhang, Z. Chang, E. Schlangen, B. Šavija, Predicting micromechanical properties of cement paste from backscattered electron (BSE) images by computer vision, Mater. Des. 229 (2023) 111905.
[26] H.K. Kim, H.K. Lee, Autogenous shrinkage reduction with untreated coal bottom ash for high-strength concrete, ACI Mater. J. 113(3).
[27] ASTM, Standard Practice for Maintaining Constant Relative Humidity by Means of Aqueous Solutions, 2012.
[28] T.R. Gyawali, Effect of the mixing procedure on the properties of lightweight EPS mortar, J. Build. Eng. 68 (2023) 106012.
[29] J. Ye, F. Teng, J. Yu, S. Yu, H. Du, D. Zhang, S. Ruan, Y. Weng, Development of 3D printable engineered cementitious composites with incineration bottom ash (IBA) for sustainable and digital construction, J. Clean. Prod. 422 (2023) 138639.
[30] H. Yuan, Z. Ge, R. Sun, X. Xu, Y. Lu, Y. Ling, H. Zhang, Drying shrinkage, durability and microstructure of foamed concrete containing high volume lime mud-fly ash, Construct. Build. Mater. 327 (2022) 126990.
[31] A.K.H. Kwan, Y. Li, Effects of fly ash microsphere on rheology, adhesiveness and strength of mortar, Construct. Build. Mater. 42 (2013) 137–145.
[32] S.A. Martini, M. Nehdi, Coupled effects of time and high temperature on rheological properties of cement pastes incorporating various superplasticizers, J. Mater. Civ. Eng. 21 (8) (2009) 392–401.
[33] M. Nehdi, S. Al Martini, Estimating time and temperature dependent yield stress of cement paste using oscillatory rheology and genetic algorithms, Cement Concr. Res. 39 (11) (2009) 1007–1016.
[34] A. Salam Mohammad, J.J. Biernacki, 2D stationary computational printing of cement-based pastes with time-dependent rheology, Mater. Today: Proc. (2023).
[35] ASTM, Standard Test Method for Autogenous Strain of Cement Paste and Mortar, 2009.
[36] S.A.f.M. Regulation, GB/T 11969-2020 Test Methods of Autoclaved Aerated Concrete, 2020.
[37] M.o.H.a.U.R.D.o.t.P.s.R.o. China, JT/G 266-2011 Foam Concrete, 2011.
[38] N. Jiang, Z. Ge, Y. Guan, Z. Zuo, H. Zhang, Y. Ling, B. Šavija, Experimentally validated meso-scale fracture modelling of foamed concrete, Theor. Appl. Fract. Mech. 122 (2022) 103631.
[39] Z. Ge, H. Yuan, R. Sun, H. Zhang, W. Wang, H. Qi, Use of green calcium sulphoaluminate cement to prepare foamed concrete for road embankment: a feasibility study, Construct. Build. Mater. 237 (2020).
[40] E.K.K. Nambiar, K. Ramamurthy, Fresh state characteristics of foam concrete, J. Mater. Civ. Eng. 20 (2) (2008) 111–117.
[41] E.K.K. Nambiar, K. Ramamurthy, Influence of filler type on the properties of foam concrete, Cement Concr. Compos. 28 (5) (2006) 475–480.
[42] Y. Song, J. Xiang, W. Cui, G. Xiong, Anhydrous ethanol as a medium used to grind soda-lime glass for cement-based materials preparation: evaluating its rheological behavior by the Herschel–Bulkley and Modified–Bingham models, J. Build. Eng. 63 (2023) 105553.
[43] R. Mandal, S.K. Panda, S. Nayak, Rheology of concrete: critical review, recent advancements, and future prospectives, Construct. Build. Mater. 392 (2023) 132007.
[44] L.U.D. Tambara Júnior, G.T. dos Santos Lima, L. Silvestro, A.S. Ruviaro, P.J.P. Gleize, A.R.G. de Azevedo, Influence of polycarboxylate superplasticizer and calcium sulfoaluminate cement on the rheology, hydration kinetics, and porosity of Portland cement pastes, J. Build. Eng. 68 (2023) 106120.
[45] W. Liu, X. Liu, L. Zhang, Y. Wan, H. Li, X. Jiao, Rheology, mechanics, microstructure and durability of low-carbon cementitious materials based on circulating fluidized bed fly ash: a comprehensive review, Construct. Build. Mater. 411 (2024) 134688.
[46] B. Klemczak, J. Gołaszewski, G. Cygan, A. Smolana, M. Gołaszewska, Shrinkage strains development in ultralight cementitious foams with embedded MPCM, Developments in the Built Environment 17 (2024) 100299.
[47] L. Zhu, Investingation on Mechanical Properties and Shrinkage of Highstrength Foam Concrete, HUnan Unirversity, 2022.
[48] Z. Zhou, Effects of Fiber and Admixture on Shrinkage Performance of Foamed Concrete, Hunan University, 2019.
[49] D. Snoeck, O.M. Jensen, N. De Belie, The influence of superabsorbent polymers on the autogenous shrinkage properties of cement pastes with supplementary cementitious materials, Cement Concr. Res. 74 (2015) 59–67.
[50] P. Lura, Autogenous Deformation and Internal Curing of Concrete, Delft University of Technology, 2003.
[51] Y.-L. Liu, C.-F. Li, H.-X. Zhai, M. Riaz Ahmad, D. Guo, J.-G. Dai, Production and performance of CO2 modified foam concrete, Construct. Build. Mater. 389 (2023) 131671.
[52] C. Sun, Y. Zhu, J. Guo, Y. Zhang, G. Sun, Effects of foaming agent type on the workability, drying shrinkage, frost resistance and pore distribution of foamed concrete, Construct. Build. Mater. 186 (2018) 833–839.
[53] J.M. Abdalhmid, A.F. Ashour, T. Sheehan, Long-term drying shrinkage of self-compacting concrete: experimental and analytical investigations, Construct. Build. Mater. 202 (2019) 825–837.
[54] Q. Wang, Z. Li, Y. Zhang, H. Zhang, M. Zhou, Y. Fang, Influence of coarse coal gangue aggregates on elastic modulus and drying shrinkage behaviour of concrete, J. Build. Eng. 32 (2020) 101748.
[55] M. Hong, D. Lei, F. Zhu, P. Bai, J. He, Experimental research on aggregate restrained shrinkage and cracking of early-age cement paste, Cement Concr. Res. 172 (2023) 107246.
[56] H. Ma, C. Fu, K. Huang, E. Dai, S. Zhang, Y. Fang, J. Feng, Study on the characteristics of alkali-activated fly ash-slag improved by cenosphere: hydration and drying shrinkage, Construct. Build. Mater. 372 (2023) 130822.
[57] G. Li, H. Tan, X. He, J. Zhang, X. Deng, Z. Zheng, Y. Guo, The influence of wet ground fly ash on the performance of foamed concrete, Construct. Build. Mater. 304 (2021) 124676.
[58] Z. Wu, S. Xie, Z. Ji, C. Ma, T. Si, J. Wu, J. Wang, Novel lightweight cement-based materials foaming by secondary aluminum ash: microwave absorption, mechanical and thermal insulation properties, Construct. Build. Mater. 413 (2024) 134328.

[59] Z. Huang, T. Zhang, Z. Wen, Proportioning and characterization of Portland cement-based ultra-lightweight foam concretes, Construct. Build. Mater. 79 (2015) 390–396.
[60] Z.P. Bažant, M.T. Kazemi, Size effect in fracture of ceramics and its use to determine fracture energy and effective process zone length, J. Am. Ceram. Soc. 73 (7) (1990) 1841–1853.
[61] M. Amran, G. Murali, N. Makul, W.C. Tang, A. Eid Alluqmani, Sustainable development of eco-friendly ultra-high performance concrete (UHPC): cost, carbon emission, and structural ductility, Construct. Build. Mater. 398 (2023) 132477.
[62] N.S. Ha, S.S. Marundrury, T.M. Pham, E. Pournasiri, F. Shi, H. Hao, Effect of grounded blast furnace slag and rice husk ash on performance of ultra-high-performance concrete (UHPC) subjected to impact loading, Construct. Build. Mater. 329 (2022) 127213.
[63] P. Yu, R.J. Kirkpatrick, B. Poe, P.F. McMillan, X. Cong, Structure of calcium silicate hydrate (C-S-H): near-, mid-, and far-infrared spectroscopy, J. Am. Ceram. Soc. 82 (3) (2004) 742–748.
[64] I. Garcia-Lodeiro, A. Palomo, A. Fernández-Jiménez, D.E. Macphee, Compatibility studies between N-A-S-H and C-A-S-H gels. Study in the ternary diagram Na2O–CaO–Al2O3–SiO2–H2O, Cement Concr. Res. 41 (9) (2011) 923–931.
[65] F. Ridi, E. Fratini, S. Milani, P. Baglioni, Near-infrared spectroscopy investigation of the water confined in tricalcium silicate pastes, J. Phys. Chem. B 110 (33) (2006) 16326–16331.
[66] Y.q. Shi Caijun, Testing and Analysis Methods for Cement-Based Materials, China Architecture & Building Press, Beijing, 2022.
[67] T.L. Lian Huizhen, Chen Enyi, Fundamentals of Physical Phase Research on Building Materials, Tsinghua University press, Beijing, 1996.
[68] X. Pu, Investigation on pozzolanic effect of mineral additives in cement and concrete by specific strength index, Cement Concr. Res. 29 (6) (1999) 951–955.